LITHOS 504-505 (2025) 108033

Contents lists available at ScienceDirect

LITHOS

journal homepage: www.elsevier.com/locate/lithos

CaREE-fluorcarbonates: A variety of morphologies, compositions and nanostructures with insights into REE partitioning and mobility

Roberto Conconi [a,b,*], Paolo Gentile [a], Patrizia Fumagalli [c], Fernando Nieto [d], Giancarlo Capitani [a]

[a] Department of Earth and Environmental Sciences, University of Milano-Bicocca, Piazza della Scienza 4, Milano 20126, Italy
[b] Université de Lille, CNRS, INRAE, Centrale Lille, UMR 8207-UMET-Unité Matériaux et Transformations, Lille, France
[c] Department of Earth Sciences "Ardito Desio", University of Milano, Via Botticelli 23, Milano 20133, Italy
[d] Departamento de Mineralogia y Petrologia and IACT, Universidad de Granada, CSIC, Granada 18002, Spain

ARTICLE INFO

Keywords:
Bastnäsite
Synchysite
Nanoparticles
Transmission electron microscopy
Raman spectroscopy
Rare earth elements

ABSTRACT

A variety of CaREE-fluorcarbonates with differing morphologies and compositions have been studied: i) synchysite-(Ce) forming hexagonal prisms and rosette-like aggregates; ii) bastnäsite-(Ce) forming blocky aggregates; iii) bastnäsite-(Nd) forming desert rose-like intergrowths and iv) combinations of synchysite-(Ce) and bastnäsite-(Nd) forming more complex micro and nanostructures. These minerals are retained to form from a hydrothermal fluid in a temperature range between 350 and 100 °C. After an investigation spanning from the microscale to the atomic scale, which employed optical stereomicroscopy, scanning and transmission electron microscopy, microanalysis and Raman spectroscopy, a possible scenario for their formation has been depicted. It is assumed that the different CaREE-fluorcarbonates crystallized sequentially under decreasing temperature and fluid fractionation, with synchysite-(Ce) forming first, followed by bastnäsite-(Ce) and finally bastnäsite-(Nd). The different morphologies, in this case, besides being influenced by the dominant REE in the fluid, were also due to varying temperatures and cooling rates.

Our study highlights that nature may efficiently fractionate REE from one another, like Y from La, Ce and Nd; Ce from Nd and La. Additionally, Th, a radioactive and toxic element, seems to enter the structure of CaREE-fluorcarbonates during the final stages of crystallization. The understanding of these natural processes may suggest routes for improving current metallurgical separation processes.

1. Introduction

Bastnäsite [$REECO_3F$] and synchysite [$CaREE(CO_3)_2F$] are end-members of the homologous polysomatic series and also economic minerals of rare earth elements (REEs). Notable intermediate ordered terms are parisite [$CaREE_2(CO_3)_3F_2$] and röntgenite [$Ca_2REE_3(CO_3)_5F_3$]. Other, rarer intermediate members have been observed, but never fully characterized (Capitani, 2019, 2020; Ciobanu et al., 2017; Meng et al., 2001a, 2001b, 2002; Van Landuyt and Amelinckx, 1975; Wu et al., 1998).

REEs are critical raw materials and their supply is crucial for the industrial progress, the development of modern technologies and environmental-friendly green technologies (Sovacool et al., 2020; Vidal et al., 2013). REEs are a set of seventeen metallic elements. These include the fifteen lanthanides on the periodic table plus scandium and yttrium. They are usually divided into two subcategories due to their similar chemical properties: light rare earth elements (LREEs), with atomic numbers 57–64, and heavy rare earth elements (HREEs), with atomic numbers 65–71. Scandium (atomic number 21) and Yttrium (39), which are not a REEs, are usually included among the HREEs due to their similar geochemical affinity. However, despite the importance of REEs, a lot of unanswered questions about the mechanisms that govern their transport and deposition in natural systems survive. The main reasons are the difficulty of reproducing in the laboratory the complex natural conditions in which they occur and that of separating different REEs, due to their similar geochemical behaviour. The understanding of such mechanisms may reveal important, not only for the geological exploration and the beneficiation of metallurgical processes, but also for the recycling of REEs, which now is under 1 %, mainly because actual methods are expensive, energy-consuming and

* Corresponding author at: Université de Lille, CNRS, INRAE, Centrale Lille, UMR 8207-UMET-Unité Matériaux et Transformations, Lille, France.
E-mail address: roberto.conconi@univ-lille.fr (R. Conconi).

https://doi.org/10.1016/j.lithos.2025.108033
Received 17 September 2024; Received in revised form 14 February 2025; Accepted 28 February 2025
Available online 3 March 2025
0024-4937/© 2025 The Authors. Published by Elsevier B.V. This is an open access article under the CC BY license (http://creativecommons.org/licenses/by/4.0/).

inefficient (Balaram, 2019; Peiravi et al., 2021).

As a matter of fact, some of the most important REEs deposits worldwide are of hydrothermal origin, i.e. hydrothermal fluids can mobilize REEs (Wang et al., 2020). Different studies that model the behaviour of REEs in hydrothermal fluids exist and all of them agree that the capacity to mobilize REEs depends on the concentration of ligands (Cl^-, F^-, CO_3^{2-}, etc.) in the fluids and on the stability of the REE-ligand complexes (Migdisov and Williams-Jones, 2014; Williams-Jones et al., 2012; Xing et al., 2019). Moreover, despite their similar geochemical behaviour, the chemical properties of REEs vary with their atomic weight and this is sufficient to partition REEs during their transport and deposition (Migdisov et al., 2016). Other factors that could influence the transport, deposition and fractionation are the interaction with the wall rocks and the consequent changing in pH (Ngwenya, 1994).

It is universally recognized, as well as often forgotten, that fundamental research is the nourishment of applied research. Indeed, mineralogical and crystallographic studies on CaREE-fluorcarbonates may shed light on their nature and genesis, eventually suggesting more successful prospection routes, enhanced metallurgical processes and recycling strategies. Particularly, the study of polysomatism may reveal important since the intergrowths of different polysomes may indicate changes in the crystallization conditions or fluid composition (Gysi and Williams-Jones, 2015). In this context, we studied, for the first time, CaREE-fluorcarbonates from miarolitic cavities of the Granophyre of Cuasso al Monte (Western Southern Alps). We found different types of CaREE-fluorcarbonates, differing by morphology, microstructure and REEs content. These findings allowed us to speculate about the crystallization pathways of these minerals and the partitioning of REEs in natural hydrothermal fluids.

2. Geological setting

Cuasso al Monte is located in the Western Southern Alps (Fig. 1). This region is renowned for the extraction of "Red Porphyry", a granophyre dimension stone, which is quarried since 1880 (Fagnani, 1946) and very appreciated mainly in the building industries for its reddish/pinkish colour and hardness. The genesis of this rock is associated with the post-Hercynian calc-alkaline magmatism that generated the "Graniti dei Laghi": felsic plutons which intruded the amphibolites and the ortho- and paragneisses of the "Serie dei Laghi" unit (Bakos et al., 1990; Boriani et al., 1988; Pinarelli et al., 1993). The granophyre represents a subvolcanic complex formed during crustal extension that was triggered by a post-orogenic regime. During this event, a mantle derived magma was emplaced at lower depth and got crustal contaminated (Bakos et al., 1990; Pinarelli et al., 2002).

The Red Porphyry shows a medium grain size and is mainly composed by K-feldspar, quartz, albite and biotite. A notable characteristic of this rock is the abundant presence of miarolitic cavities, which were filled with secondary minerals by the circulation of late hydrothermal fluids (Pezzotta et al., 1999). Hydrothermal activity was responsible for both the crystallization of tens of different mineral species (Capitani et al., 2018; Demartin et al., 2001; Pezzotta, 2005; Pezzotta et al., 1999; Vignola et al., 2012), and the alteration of the rock forming minerals (such as the alteration of K-feldspar and the chloritization of biotite). The CaREE-fluorcarbonates studied here come from these miarolitic cavities, which also host feldspar, quartz, fluorite, chamosite, sphalerite, anatase, aeschynite and zircon (Capitani et al., 2018).

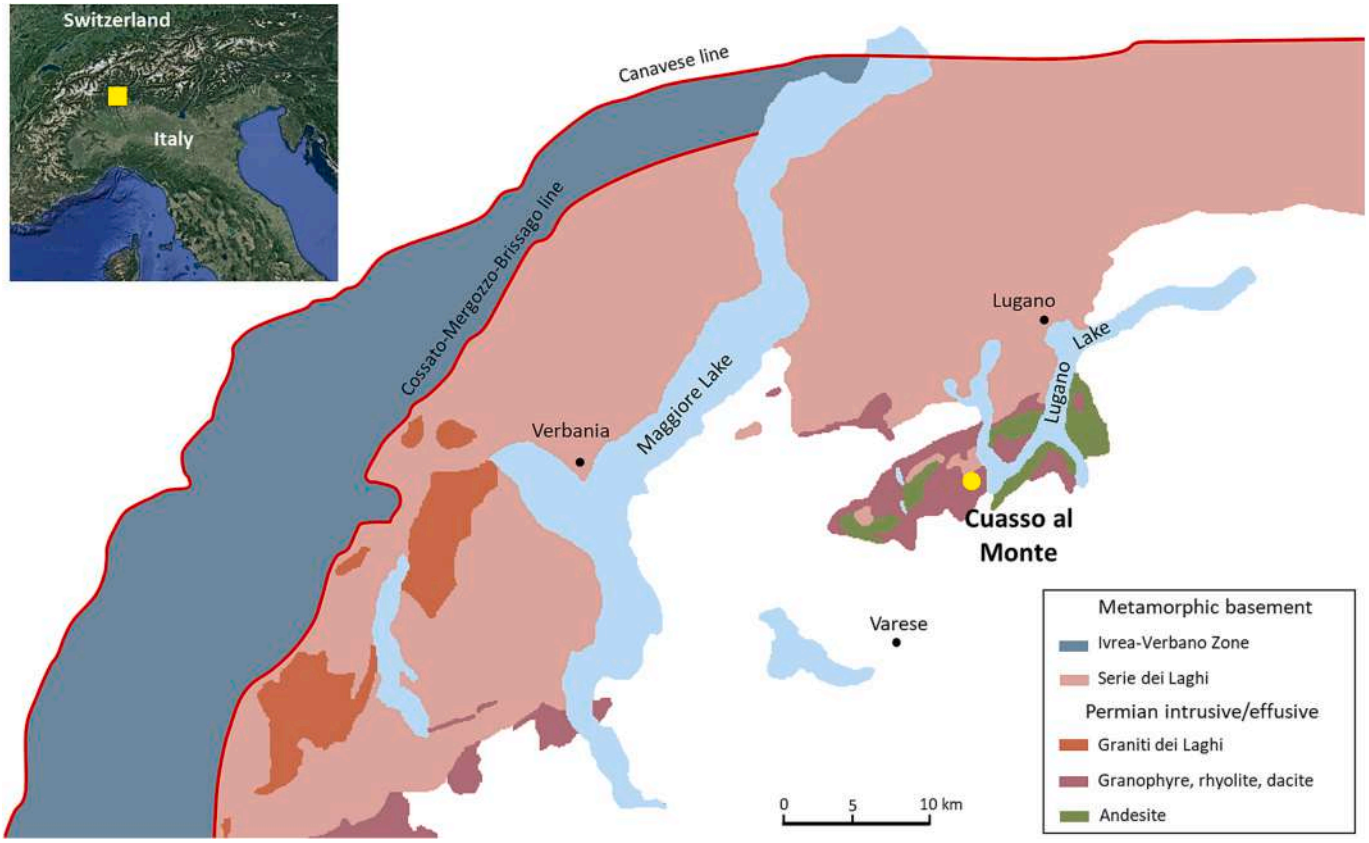

Fig. 1. Simplified geological map of the Hercynian plutonic and volcanic rocks in the Western Southern Alps. Yellow dots indicate the locality where the CaREE-fluorcarbonates were collected (modified from Capitani et al., 2018). (For interpretation of the references to colour in this figure legend, the reader is referred to the web version of this article.)

3. Samples and methods

The CaREE-fluorcarbonates occur in three different morphologies: i) rosette-like aggregates, which are formed by hexagonal lamellae (Fig. 2A, B): ii) hexagonal prisms aggregates (Fig. 2C, D) and iii) blocky subhedral aggregates (Fig. 2E, F). Crystal aggregates are generally less than 400 μm, whereas single prisms are less than 100 μm in diameter. All aggregates show a yellowish to reddish colour, but hexagonal prisms, which may occur either as individual crystals or aggregates, are frequently zoned, with a light red rim and a dark red core. The CaREE-fluorcarbonates can be found on K-feldspar, chamosite, fluorite and quartz; less frequently included in quartz and fluorite.

Before instrumental analysis with Raman spectroscopy and scanning electron microscopy (SEM), the samples were embedded in epoxy resin and then polished using alumina with a nominal grain diameter of 0.3 μm as the last polishing step. The samples were carbon coated with a 20 nm C-film before energy dispersive spectroscopy (EDS) SEM analysis; the C-film was not present during Raman analysis.

Micro-Raman spectroscopy was carried out at the Department of Earth Science "Ardito Desio" of the University of Milan using a LabRAM HR Evolution. Scattered light, excited by the 633 nm/17mw emission of a He/Ne laser source, was collected at room temperature using a 50× objective. Extended spectra were collected with a 600 grooves/mm diffraction grating, while a 1800 grooves/mm grating was used for higher spectral resolution in the spectra collected around the $v_1(CO_3^{2-})$ region. Spectra were detected by a Peltier-cooled Charge Couple Detector (CCD). To optimize signal to noise ratio, three accumulations of 30 s each were collected at each point. The system was calibrated using the 520.7 cm^{-1} line of a silicon wafer. All spectra were collected close to SEM analyses, allowing a comparison of results. Spectra fitting benefitted of background subtraction assuming Lorentzian band shapes.

SEM-EDS observations were carried out at the Platform of Microscopy of the University of Milano-Bicocca (PMiB) with a field emission gun (FEG) SEM Zeiss Gemini 500, operating at 15 keV and equipped with a Bruker QUANTAX integrated wave-dispersive/energy-dispersive (WDS/EDS) system. The standard method and φ(ρz) correction were used for quantitative analysis (Newbury and Ritchie, 2015; Newbury and Ritchie, 2019; Pouchou and Pichoir, 1991). The following natural minerals, synthetic compounds and pure metals were used as standard: CeO_2 (Ce), LaF_3 (La, F), $NdSi_2$ (Nd), Sm (Sm), Y (Y), $PrSi_2$ (Pr), Gd (Gd), ThF_4 (Th), hematite (Fe), chlorite (Si, Al and Fe), and synchysite (Ca). The final (tabled) analyses were obtained with EDS, since the much higher current required by WDS (~20 nA) compared with EDS (~200 pA), damaged the delicate CaREE-fluorcarbonates.

To shed light on the complexity detected by micro-Raman spectroscopy and SEM-EDS in rosette-like fluorcarbonates (see "Results" section), transmission electron microscopy (TEM) observations were conducted. TEM mounts were obtained by cutting slices approximately 70 nm thick using a Leica Ultracut E ultramicrotome.

TEM observations were performed both at the PMiB, using a Jeol JEM2100Plus, and at the Centro de Instrumentacion Cientifica (CIC) of the University of Granada, using a FEI TITAN G2. The Jeol is supplied with a LaB_6 source, operates at 200 kV, and is equipped with an Oxford EDS system and a Gatan Rios CMOS camera. The FEI is supplied with a Schottky FEG, operated at 300 kV, and is equipped with a C_s-corrector, a FEI 4 in-column SDD Super-X EDS detector and a high angle annular dark field (HAADF) detector for scanning transmission electron microscopy (STEM) observations.

TEM-EDS analyses were collected with the Jeol (PMiB) and quantified using Aztec (Oxford) software. Analyses of CaREE-fluorcarbonates were quantified with the standardless method and corrected for absorption (Conconi et al., 2023b). Analyses of phyllosilicates were quantified with the Cliff-Lorimer approximation and did not require correction for absorption.

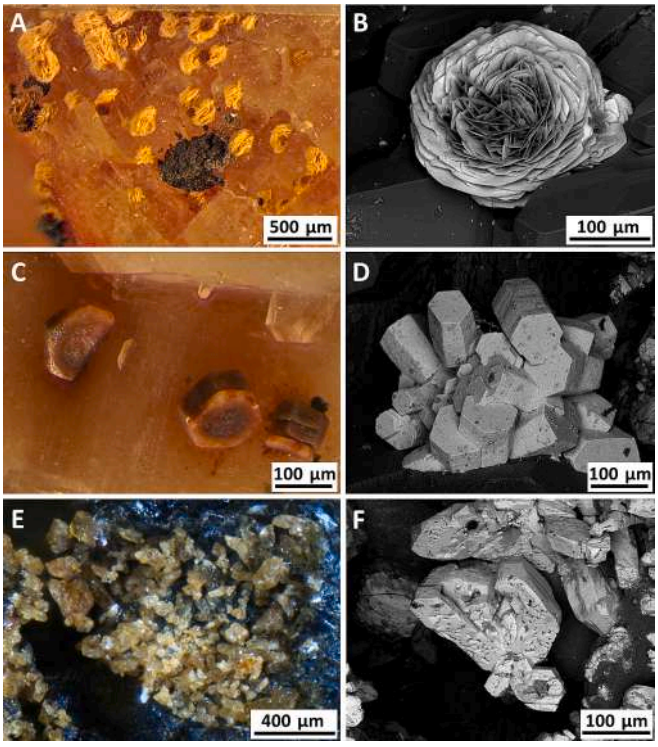

Fig. 2. Optical micrographs and SEM (SE) images showing (A, B) rosette-like, (C, D) hexagonal prisms and (E, F) blocky subhedral aggregates of CaREE-fluorcarbonates.

4. Results

4.1. Hexagonal prisms aggregates: Synchysite-(Ce)

Raman spectroscopy and SEM-EDS both identify the hexagonal prisms aggregates as synchysite-(Ce). Backscattered electron (BSE) images show a core-rim zoning, consistently with optical observations (Fig. 3). EDS analyses show an average Ca/(Ca + REE) ratio close to 0.50, clearly indicating synchysite-(Ce) (Table 1). EDS maps reveal that zoning concerns the distribution of Ce, La, Nd, Y and Th, with the rim enriched in Y and the outer rim in Th and both depleted in Ce, La and Nd compared to the core (Fig. 3). Gd, Pr and Sm do not vary significantly from core to rim. Micro-inclusions of Fe-oxides and thorite were detected at the rim. Raman spectra show the typical vibrational modes of the carbonate group (CO_3^{2-}): the symmetric stretching [$v_1(CO_3)$], the antisymmetric stretching [$v_3(CO_3)$] and the in-plane bending [$v_4(CO_3)$] vibrations were observed at 1080–1100 cm^{-1}, ~1440 cm^{-1} and 730–770 cm^{-1}, respectively. Moreover, the symmetric stretching vibration [$v_1(CO_3^{2-})$] shows the characteristic double splitting typical of synchysite (Fig. 4) with bands at 1082 and 1098 cm^{-1}, in agreement with Conconi et al. (2023a).

4.2. Subhedral blocky aggregates: Bastnäsite-(Ce)

SEM-EDS analyses of subhedral blocky aggregates do not reveal any zoning or intergrowths with other phases (Fig. 5A). The Ca/(Ca + REE) ratio and the REEs sum are 0.01 and 0.98 respectively, with Ce as the dominant REE, suggesting bastnäsite-(Ce) (Table 1). Other major REEs are La and Nd, whereas Sm, Pr, Gd and Y are present as minor components.

The Raman analysis shows the v_1, v_3 and v_4 vibrational modes of the (CO_3^{2-}) group and the $v_1(CO_3)$ symmetric stretching vibration centred at 1095 cm^{-1}, as for bastnäsite-(Ce) (Conconi et al., 2023a) (Fig. 5B), therefore confirming SEM-EDS results.

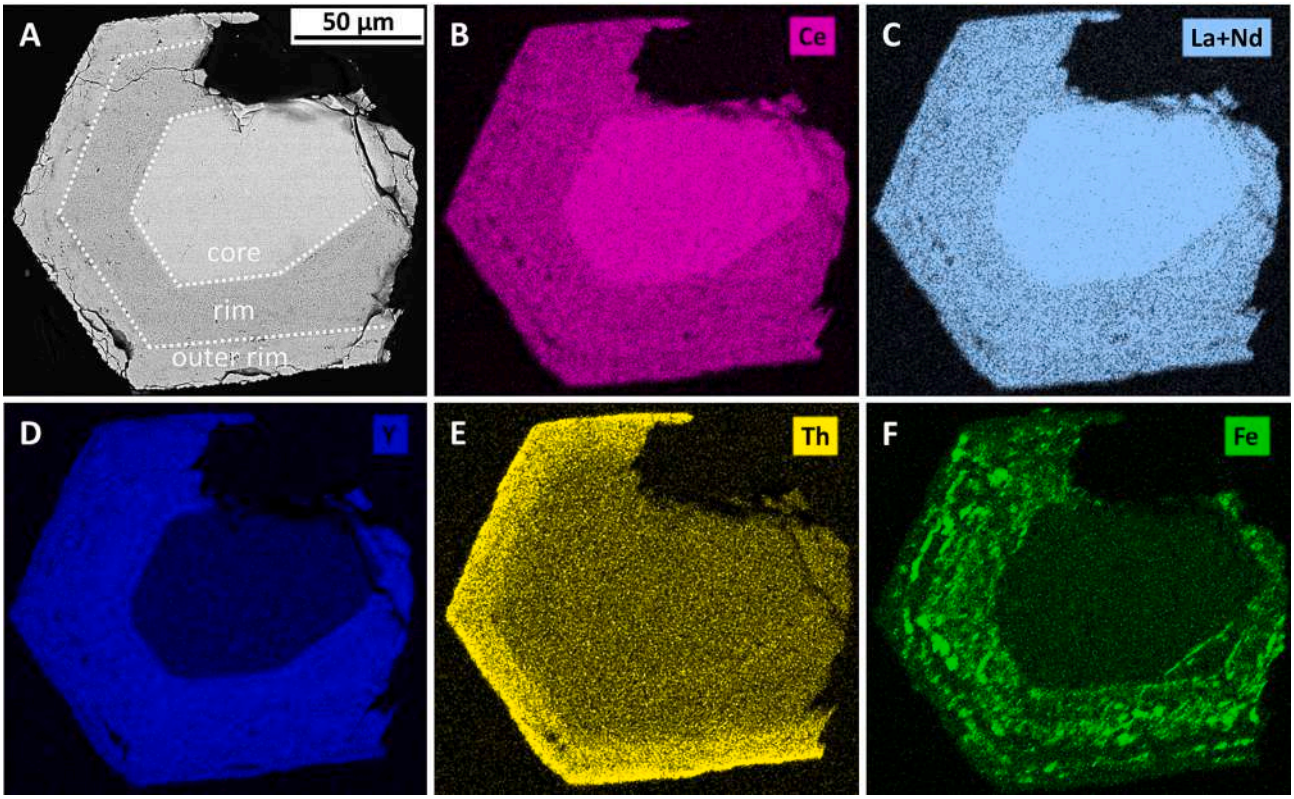

Fig. 3. A) BSE image showing the zonation of a hexagonal prism of synchysite-(Ce). B, C, D, E and F) EDS maps showing the partitioning of Ce, La, Nd, Y, Th and Fe.

Table 1
SEM- and TEM-EDS analyses (a.p.f.u.) of synchysite (Syn) and bastnäsite (Bsn). Number of analyses and standard deviations in square and round brackets, respectively. Standard deviations in italics when larger than the attached values, meaning that most of the averaged values are below the detection limit (*b.d.l.*) whereas some have relatively high values. The a.p.f.u. were recalculated on the basis of one cation for bastnäsite and two cations for synchysite.

	SEM-EDS								TEM-EDS				
	Hexagonal prism			Blocky	Rosette like aggregates								
	Syn-(Ce) core [13]	Syn-(Ce) rim [15]	Syn-(Ce) out-rim [15]	Bsn-(Ce) [13]	Syn-(Ce) [21]	Syn-Y-poor [5]	Th-rich tips [3]	Porous rim [7]	Bsn-(Nd) [20]	Syn-(Ce) [27]	Syn-Y-poor [4]	Bsn-(Nd) [12]	Porous rim [11]
F	0.510 (0.009)	0.823 (0.182)	0.779 (0.232)	0.906 (0.045)	0.640 (0.197)	1.079 (0.034)	1.008 (0.032)	1.168 (0.191)	0.766 (0.196)	1.007 (0.147)	0.920 (0.070)	1.249 (0.139)	1.186 (0.170)
Ca	0.993 (0.010)	1.025 (0.021)	1.033 (0.017)	0.010 (0.003)	1.017 (0.014)	0.982 (0.032)	1.181 (0.031)	0.902 (0.025)	0.138 (0.028)	0.989 (0.064)	0.914 (0.035)	0.086 (0.007)	0.212 (0.040)
Y	0.038 (0.009)	0.266 (0.031)	0.233 (0.025)	0.023 (0.010)	0.179 (0.032)	0.035 (0.013)	0.340 (0.018)	0.131 (0.007)	0.095 (0.034)	0.143 (0.055)	0.041 (0.044)	0.114 (0.014)	0.035 (0.012)
La	0.108 (0.007)	0.085 (0.015)	0.062 (0.004)	0.182 (0.023)	0.149 (0.029)	0.235 (0.023)	0.037 (0.011)	0.215 (0.013)	0.209 (0.012)	0.189 (0.032)	0.252 (0.022)	0.233 (0.022)	0.245 (0.037)
Ce	0.443 (0.016)	0.317 (0.024)	0.301 (0.013)	0.504 (0.015)	0.373 (0.040)	0.535 (0.008)	0.127 (0.026)	0.245 (0.027)	0.150 (0.023)	0.396 (0.067)	0.548 (0.034)	0.214 (0.016)	0.135 (0.073)
Nd	0.258 (0.007)	0.167 (0.008)	0.163 (0.006)	0.176 (0.014)	0.167 (0.014)	0.137 (0.007)	0.079 (0.013)	0.222 (0.013)	0.243 (0.017)	0.189 (0.032)	0.171 (0.013)	0.263 (0.022)	0.204 (0.023)
Th	0.005 (0.002)	0.010 (0.006)	0.080 (0.015)	0.015 (0.002)	*0.004 (0.006)*	*b.d.l*	0.154 (0.013)	0.160 (0.020)	0.044 (0.006)	*0.016 (0.032)*	*b.d.l*	0.034 (0.006)	0.140 (0.042)
Pr	0.074 (0.004)	0.045 (0.002)	0.044 (0.005)	0.052 (0.004)	0.042 (0.005)	0.055 (0.002)	0.015 (0.006)	0.054 (0.004)	0.042 (0.003)	0.025 (0.022)	*0.019 (0.032)*	0.060 (0.007)	0.053 (0.018)
Sm	0.059 (0.016)	0.043 (0.006)	0.045 (0.004)	0.018 (0.004)	0.037 (0.017)	0.011 (0.003)	0.032 (0.006)	0.050 (0.014)	0.049 (0.006)	0.026 (0.019)	*b.d.l*	0.046 (0.015)	0.031 (0.007)
Gd	0.029 (0.005)	0.043 (0.005)	0.039 (0.003)	0.011 (0.003)	0.031 (0.014)	0.009 (0.001)	0.036 (0.001)	0.019 (0.008)	0.030 (0.007)	0.020 (0.015)	*b.d.l*	0.039 (0.008)	*0.008 (0.009)*
Σ REE	1.007 (0.010)	0.975 (0.021)	0.967 (0.017)	0.980 (0.005)	0.983 (0.014)	0.976 (0.049)	0.818 (0.031)	1.098 (0.025)	0.862 (0.030)	0.985 (0.049)	1.031 (0.039)	1.005 (0.053)	0.851 (0.043)
Ca/(Ca + REE)	0.496 (0.005)	0.512 (0.011)	0.517 (0.009)	0.011 (0.003)	0.509 (0.007)	0.512 (0.025)	0.591 (0.016)	0.451 (0.013)	0.138 (0.013)	0.501 (0.020)	0.470 (0.018)	0.079 (0.008)	0.199 (0.030)

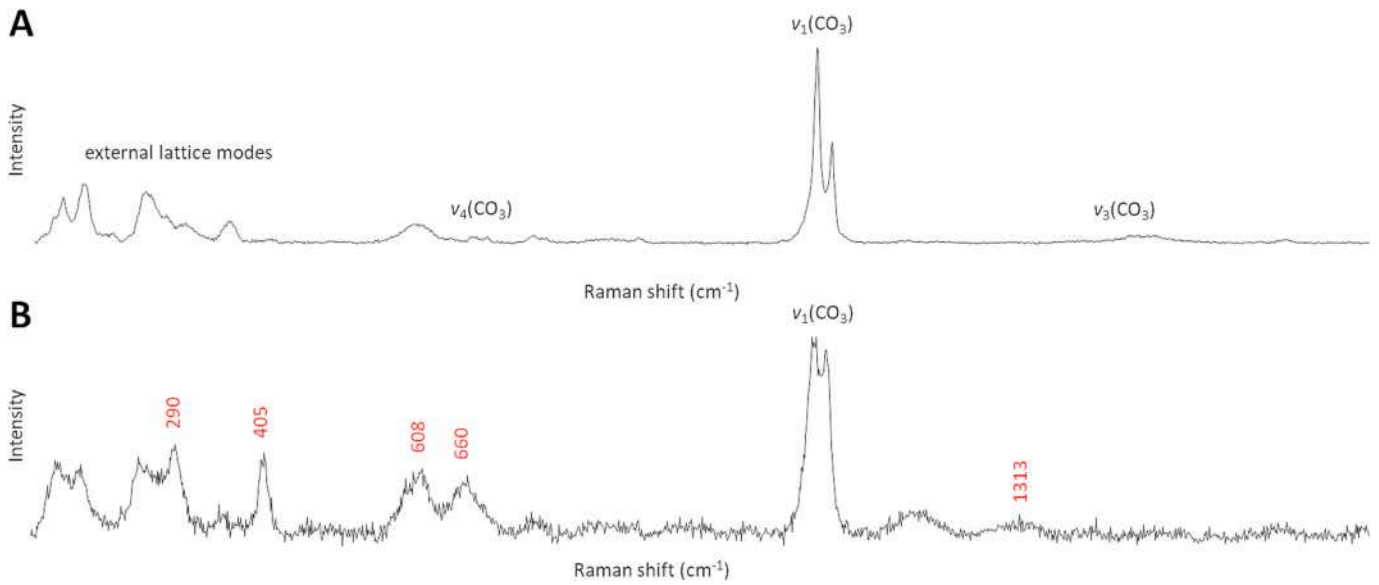

Fig. 4. Raman spectra collected at the centre (A) and at the rim (B) of the synchysite crystal. In both cases, the double splitting characterising the $v_1(CO_3^{2-})$ symmetric stretching vibration is visible. Moreover, the spectrum collected at the rim shows bands assigned to hematite (in red), a higher background and broadening of the $v_1(CO_3^{2-})$ symmetric stretching vibration. The latter suggests a loss of crystallinity at the rim due to metamictic damage caused by α-decay of Th. (For interpretation of the references to colour in this figure legend, the reader is referred to the web version of this article.)

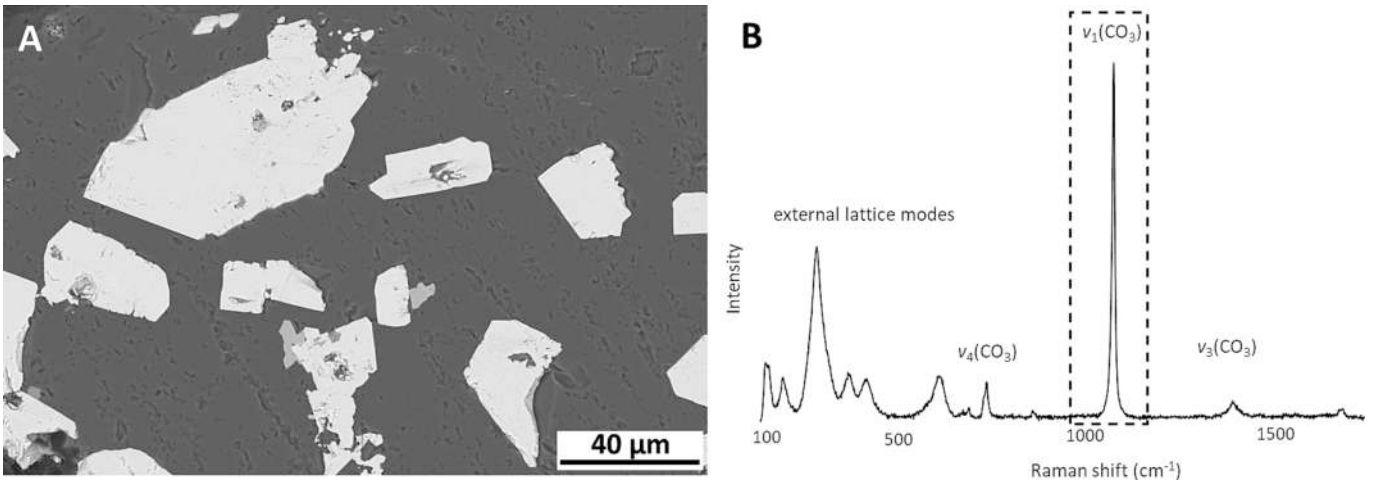

Fig. 5. (A) BSE image of subhedral blocky bastnäsite-(Ce) and (B) related Raman spectrum showing the characteristic single band of the $v_1(CO_3)$ symmetric stretching vibration.

4.3. Rosette-like aggregates: Synchysite-(Ce) and bastnäsite-(Nd)

Raman spectroscopy and quantitative EDS analysis reveal that the rosette-like CaREE-fluorcarbonates actually consist of two different species: synchysite-(Ce) and bastnäsite-(Nd). However, the analysis highlights complex microstructures, which were deeply studied by TEM.

Synchysite-(Ce) forms thick, flat and compact lamellae (Fig. 6A, B) and shows different microstructure: i) a minimal porosity concentrated at the rims (Fig. 6C), which sometimes are depleted in Ca and Ce and enriched in Si and Al with respect to the core; ii) a chemical zoning with Y-depleted regions in the core of the lamellae and Th-, Y-enriched tips, somehow resembling the chemical zoning of hexagonal prism synchysite-(Ce) described above (Fig. 6D) and iii) a porous rim enriched in Th, Nd, La, Si and Al and depleted in Ce and Ca (Fig. 6E, F). Quantitative EDS analyses of synchysite-(Ce) (Table 1) revealed a Ca/(Ca + REE) ratio of ~0.50, clearly indicating synchysite. Moreover, the samples contain Ce, Y, La and Nd as major REEs, whereas Sm, Pr and Gd are present as minor components. As for the synchysite-(Ce) hexagonal prisms, Raman spectra show the characteristic double splitting of the symmetric stretching vibration [$v_1(CO_3^{2-})$], with two bands at 1082 and 1100 cm^{-1}.

TEM-EDS analysis shows that synchysite-(Ce) has a nanostructure where rosette-like "petals" are single crystals (Fig. 7A, B) with the shortest dimension parallel to c*, the stacking direction of CaF-, Ce- and (CO_3)-layers. Each "petal" can therefore be assimilated to a stubby prism. TEM-EDS analyses (Table 1) reveal a Ca/(Ca + REE) ratio and Ca content of 0.50 and 0.99 a.p.f.u, respectively, corresponding to the ideal synchysite composition. Selected area electron diffraction (SAED) patterns and lattice fringes images reveal the presence of polysomatic and polytypic disorder (Fig. 7C, D).

The porous rim bordering synchysite-(Ce) (Fig. 6E, F) consists of bastnäsite-(Nd) nanorods, particularly enriched in Th (2.10–4.01 at.%) (Fig. 7 E, F). These show a surprisingly high Ca content (up to 0.16 a.p.f.u, Table 1), which at a first glance may be due to secondary fluorescence of surrounding synchysite, but the possibility that, at least in part, it could be in solid solution with REEs within bastnäsite cannot be entirely

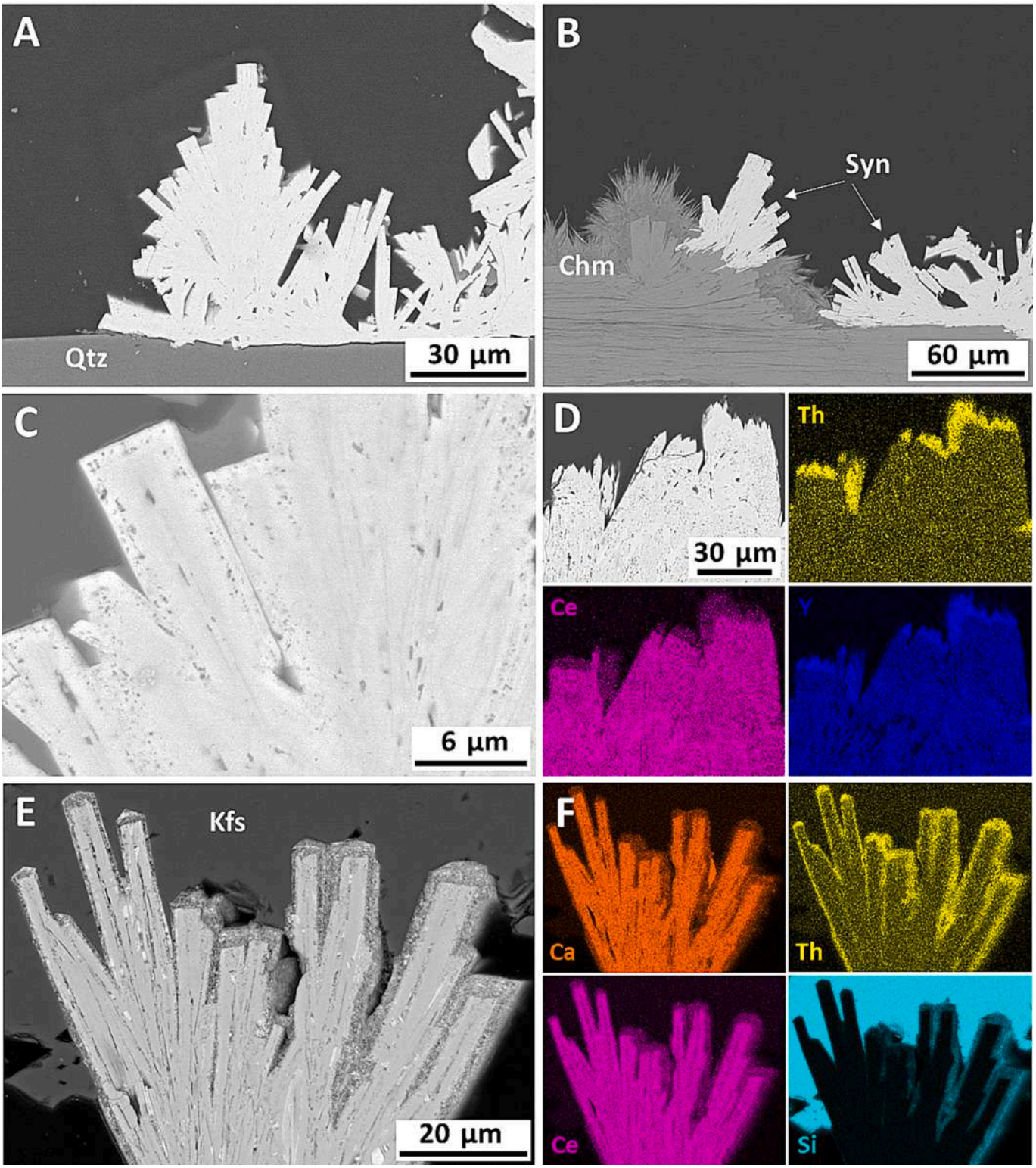

Fig. 6. BSE images showing: (A, B) thick, flat and solid lamellae of synchysite-(Ce) (Syn) on quartz (Qtz) and on two different generations of chamosite (Chm); (C) enlargement of A showing the porosity concentrated on the rim of the lamellae; (D) EDS maps showing the Y poor regions and the enrichment in Th and Y at the tips of the lamellae; (E) synchysite-(Ce) framed by a porous rim on K-feldspar (Kfs); (F) EDS map of E showing the enrichment in Th and Si and the depletion in Ca and Ce in the porous rim. Darker grey in all BSE images is the epoxy resin.

excluded (see ahead).

Bastnäsite-(Nd), in comparison with synchysite-(Ce), forms thinner and slightly bent lamellae with a widespread porosity (Fig. 8). The SEM-EDS analysis reveals a composition different from that of any other polysome of the bastnäsite-synchysite series described so far (Table 1). The Ca/(Ca + REE) ratio varies between 0.09 and 0.15, which are close to the Ca/(Ca + REE) ratio of the theoretical B_6S and B_5S polysomes, 0.12 and 0.14, respectively (Capitani, 2019). A peculiar characteristic of this phase is that Nd is the dominant REE, followed by La and Ce. Besides, Si, Al and Fe are almost always present, suggesting additional

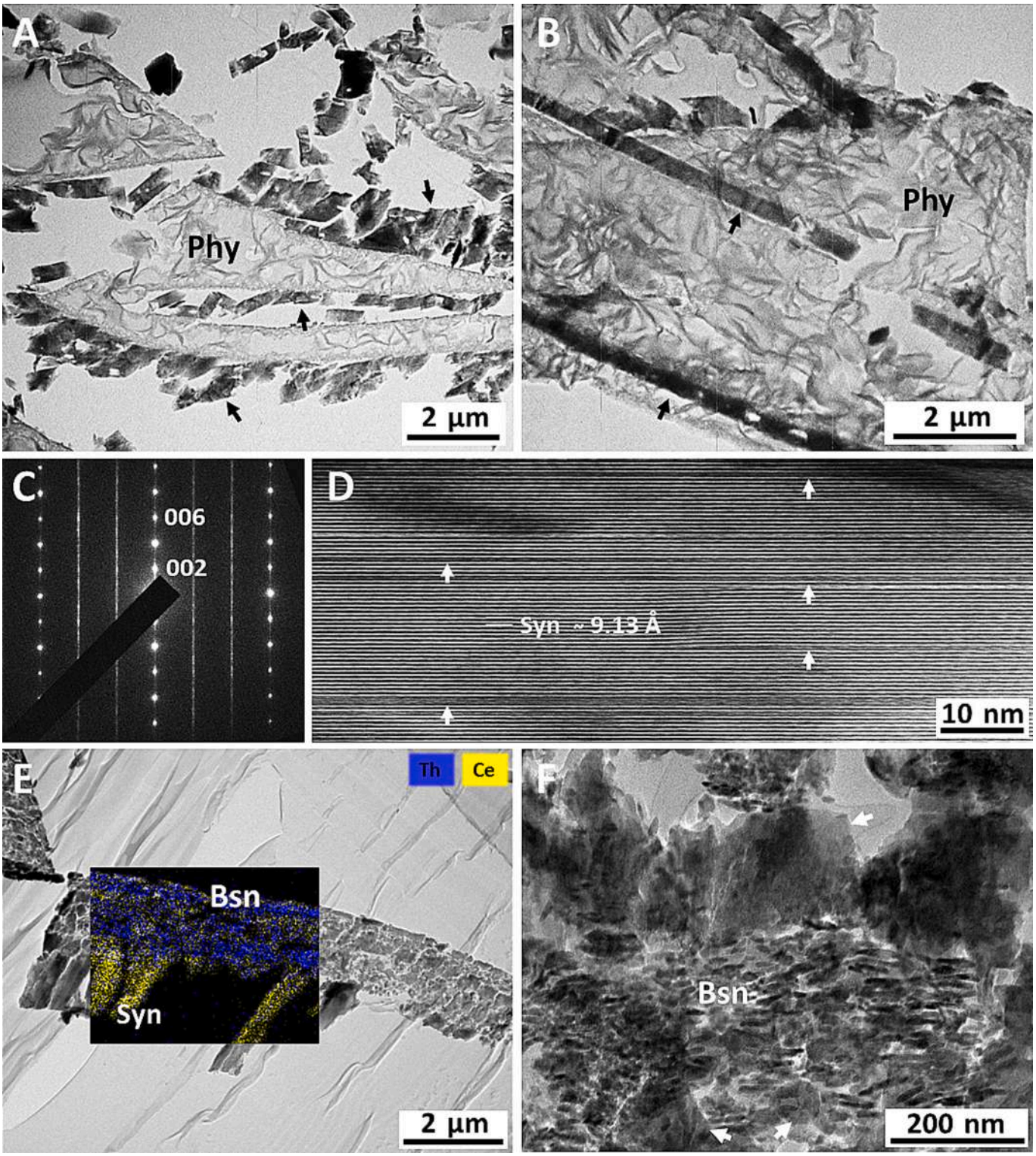

Fig. 7. (A, B) Bright field TEM images of synchysite-(Ce) lamellae (black arrows) with phyllosilicates (Phy). (C) SAED pattern of synchysite-(Ce) along [110] showing polytypic and polysomatic disorder. (D) High resolution TEM image showing Ca-poor polysomatic faults (white arrows) within synchysite-(Ce) (Syn). (E) Bright field TEM image showing the porous rim of synchysite-(Ce) with superimposed EDS map showing the enrichment in Th. (F) Enlargement of E showing the presence of bastnäsite-(Nd) nanocrystals and synchysite-(Ce) (white arrows).

phases intergrown with the CaREE-fluorcarbonate at a scale not resolvable with SEM-EDS.

On the other hand, Raman spectra show the presence of a single symmetric stretching vibration $\nu_1(CO_3^{2-})$, typical of bastnäsite (Fig. 8E). However, in the bastnäsite-(Ce) described by Conconi et al. (2023a), this band is centred at 1095 cm^{-1}, while here is observed at 1098 cm^{-1}. This Raman shift difference may derive from the different compositions of the compared bastnäsites. Indeed, the lanthanide contraction causes Nd to have a smaller ionic radius than Ce, therefore the possibility to form stronger bonds and consequently a positive Raman shift. Finally, the

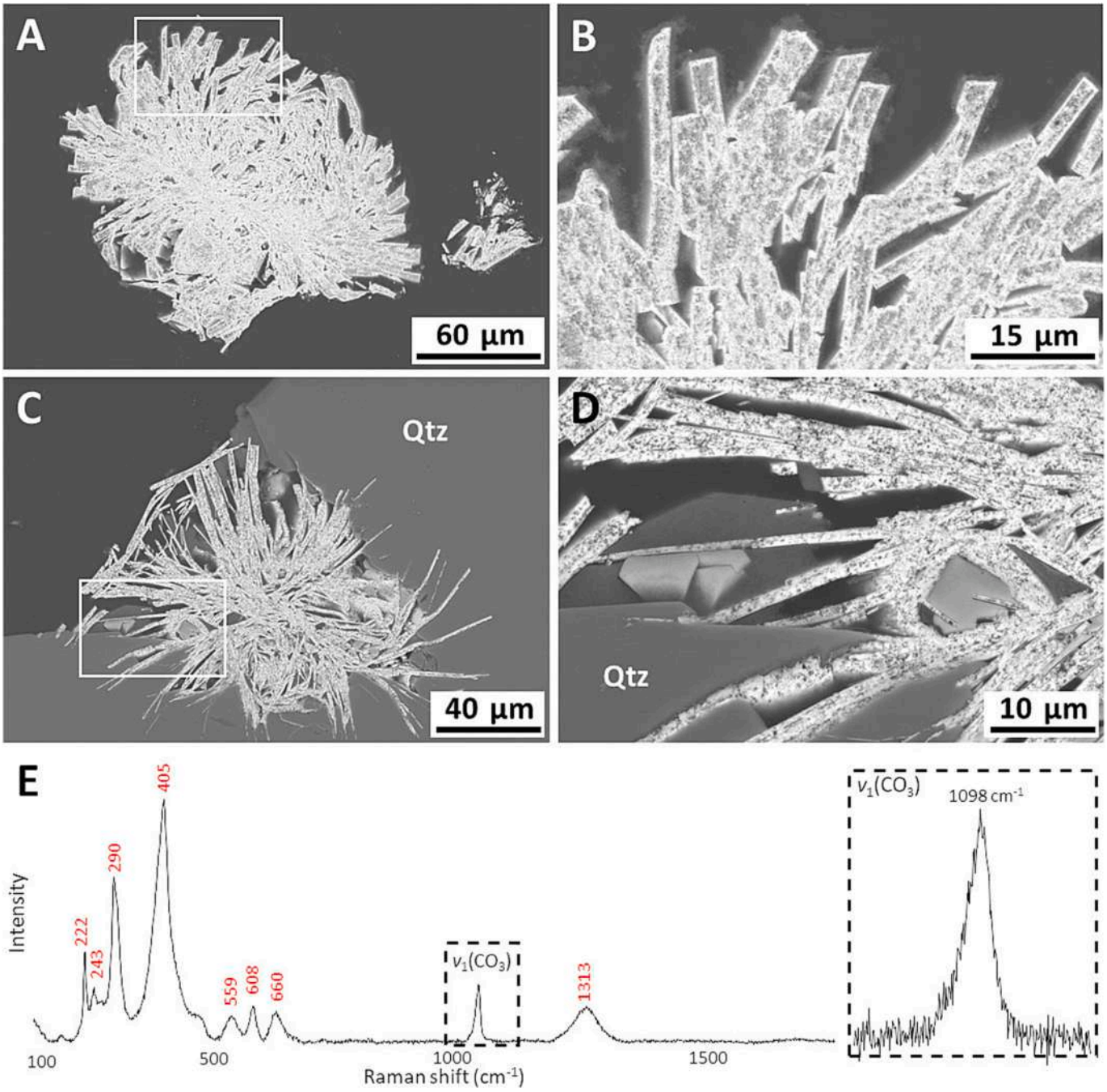

Fig. 8. BSE images showing the microstructure of rosette-like bastnäsite-(Nd) (A, C) and their enlargement showing the porous microstructure (B, D). (E) Raman spectrum of bastnäsite-(Nd), with the symmetric stretching vibration (v_1) at 1098 cm^{-1}. Moreover, bands belonging to hematite (numbers in red) were observed. (For interpretation of the references to colour in this figure legend, the reader is referred to the web version of this article.)

Raman spectra show intense bands from 222 to 660 cm^{-1}, and at 1313 cm^{-1} that can be assigned to hematite (Kuebler et al., 2006). Consequently, intergrowths of, at least, hematite and CaREE-fluorcarbonate can be inferred. At this stage, the origin of Si and Al detected by EDS remains unexplained, as well as if the observed Ca/(Ca + REE) ratio reflects ordered polysomes (B_6S or B_5S) or arises from disordered intergrowths of Ca-rich lamellae and bastnäsite. With the aim to solve these issues, we pushed the investigation at the TEM scale.

At the TEM scale, bastnäsite-(Nd) shows a complex nanostructure recalling the gypsum or calcite "desert rose" (although at smaller scale), made of an intergrowth of bastnäsite and hematite nanocrystals, with also phyllosilicates, including kaolinite-like and undefined other phases (Fig. 9A, B). The CaREE-fluorcarbonate forms nanorods generally less than 50 nm in length (Fig. 9C). Hematite was observed both as nanorods up to 200 nm in length and as irregular nanoparticles; generally, they are dispersed within bastnäsite, but sometimes form clusters. Phyllosilicates are present either along the rim of the rosette-like "petals" or within interstices left by bastnäsite-hematite intergrowths. Overall, this intergrowth constitutes the porosity observed by SEM.

TEM-EDS analyses on bastnäsite nanocrystals show a Ca/(Ca + REE) ratio of 0.08 and a REEs sum of 1.00 a.p.f.u (Table 1). No presence of Si, Al and Fe were detected as, instead, was observed in SEM-EDS, suggesting that Si and Al and part of the Fe come from phyllosilicates, and most of the Fe from hematite. Sometimes, bastnäsite-(Nd) shows a

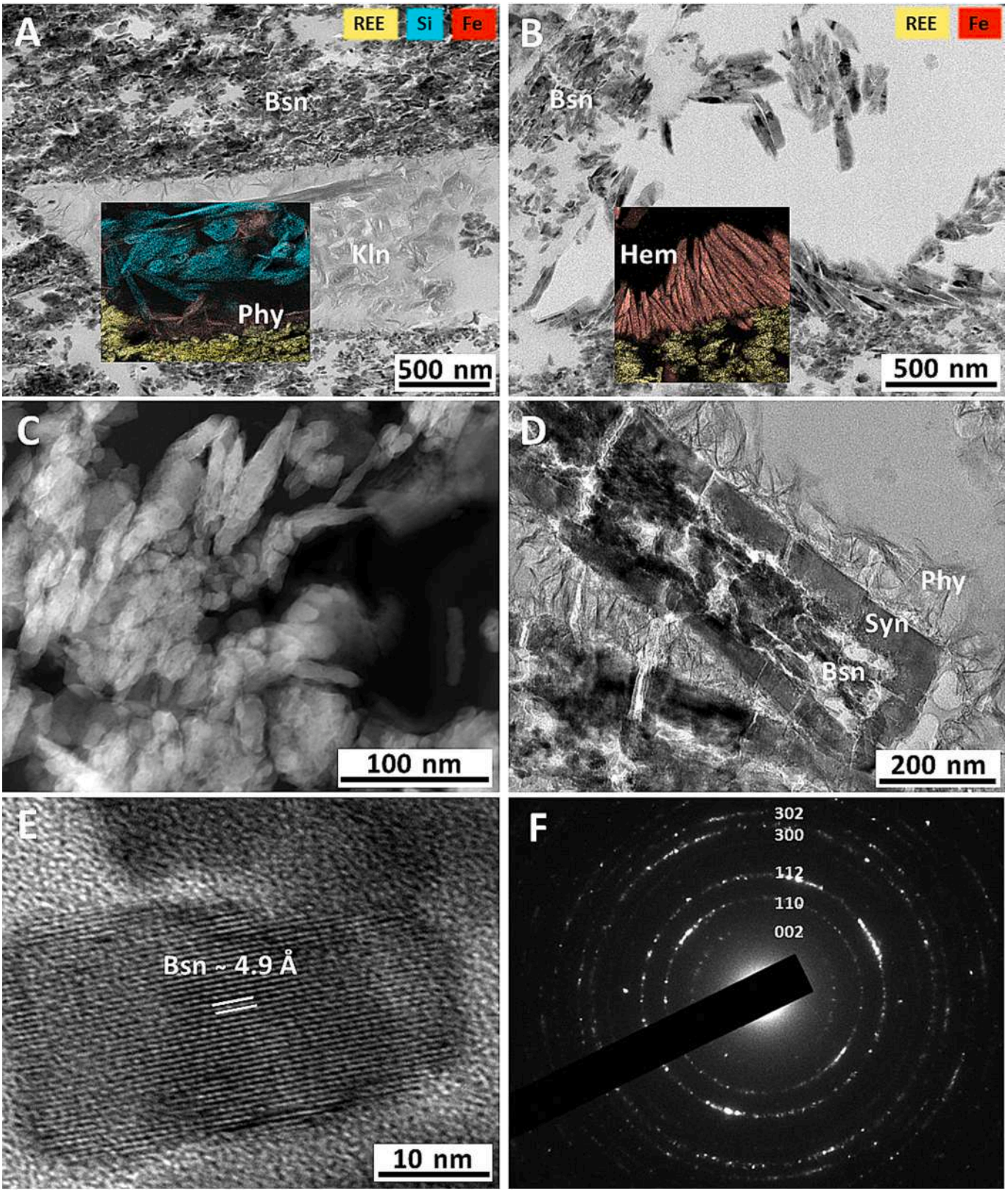

Fig. 9. Bright field TEM images with superimposed TEM-EDS maps showing: A) and B) the nanostructure of bastnäsite-(Nd) in which bastnäsite nanocrystals (Bsn) are intergrown with phyllosilicates (Phy), kaolinite-like (Kln) and hematite (Hem); C) HAADF STEM image showing the spindle shape of bastnäsite nanocrystals. D) "scaffold" nanostructure with bastnäsite nanocrystals walled by synchysite-(Ce) (Syn) and phyllosilicates (Phy). E) Lattice fringe image of bastnäsite-(Nd) showing a constant ~4.9 Å spacing. F) SAED patterns of bastnäsite nanocrystals showing the typical diffraction rings of polycrystalline materials (main rings indexed).

"scaffold" nanostructure made of a core of bastnäsite-(Nd) nanocrystals walled by solid synchysite-(Ce), in turn surrounded by phyllosilicates (Fig. 9D).

Overall, lattice fringe images and the diffraction patterns of the bastnäsite-(Nd) show an ordered structure with constant (002) d-spacing of ~4.9 Å (Fig. 9E, F), i.e. we could not ascertain the presence of Ca-bearing lamellae such as synchysite (~9.1 Å) or parisite (~14.0 Å) (in all these phases the (001) lattice fringes are forbidden by symmetry, *P*-62*c*, *Cc* and *C*2/*c*, respectively, so that only the halved periodicity is observed in HR images). Therefore, we cannot but conclude that Ca, at least in nanocrystals, can enter the bastnäsite-(Nd) structure in solid solution with REEs up to 0.08 a.p.f.u.

TEM-EDS analyses on phyllosilicates revealed the presence of at least three different species: an amorphous kaolinite-like phase and two other undefined phases (Table S1). The former shows Al and Si in almost 1:1 ratio, like for kaolinite, and the corresponding SAED patterns is typical of amorphous material (Fig. S1). Instead, the two undefined phases have a Si to Fe ratio close to 4:1 and 1:1, respectively. Other elements such as Na, K, Mg, Al and Ca are present in minor amounts. The crystal morphology unmistakably resembles phyllosilicate group minerals, and the measured lattice fringe spacing of either 14 or 16 Å may suggest chlorite- or smectite-like phases. However, SAED patterns and compositions do not unambiguously match any known phyllosilicate (Fig. S2). These phases may represent metastable clay precursors similar to those described by Tazaki (2005).

5. Discussion and conclusions

The miarolitic cavities of the granophyre of Cuasso al Monte are filled with minerals of accredited hydrothermal origin. Indeed, several authors agree that a massive fluid circulation involved a significant portion of the Serie dei Laghi, including the granophyre (Capitani et al., 2018; Demartin et al., 2001; Pezzotta, 2005; Pezzotta et al., 1999; Vignola et al., 2012). These fluids were also responsible for the alteration of K-feldspar, biotite and plagioclase. Based on the study of Sc-silicates, Pezzotta (2005) proposed two different models to explain the precipitation of rare hydrothermal phases into miarolitic cavities and both agree that CaREE-fluorcarbonates were formed as final products in a low temperature environment. REEs, as well as other elements (e.g. Ti, Nb, Ta, Sc, etc.), were made available by the activity of F-rich fluids, which have altered primary gadolinite-(Y), siderophyllite, feldspar, and other rock-forming minerals. Along the same, Capitani et al. (2018), on the basis of the textural relationships involving anatase, aeschynite and zircon from the same miarolitic cavities, depicted a scenario in which F-rich hydrothermal fluids altered primary minerals and then, on cooling, deposited accessory phases in a sequence that reflected fluids saturation and elements fractionation within a range of 250–100 °C. REE-carbonates were among the latest phases to crystallize and, in the case that hydrothermal fluids contained enough Ca^{2+} ions, synchysite was the first CaREE-fluorcarbonate to precipitate, similar to what is observed in magmatic contexts (Förster, 2001 and references therein). Indeed, it has been observed experimentally, although at higher temperatures (300–400 °C), that the relative stability field of Ca REE-fluorcarbonate (parisite in this case) compared to that of bastnäsite, is wider at high temperature than at low temperature, and expand with increasing $a(Ca^{2+})$ and $a(F^{-})$ (Gysi and Williams-Jones, 2015).

Laboratory experiments are often used to better constrain the precipitation pathway of REEs bearing minerals (i.e. REE-carbonates and REE-hydroxylcarbonates) in nature. However, a general mechanism has not been conceived yet because of the many factors intervening in the REE-carbonates precipitation under hydrothermal conditions. Among the main factors affecting crystal morphology there are the dominant REE in the system, temperature, heating rate and curing time (Price et al., 2023; Rodriguez-Blanco et al., 2014; Szucs et al., 2023; Vallina et al., 2014), as already known for other, more common carbonates such as calcite (Liendo et al., 2022).

The zoning affecting synchysite-(Ce) prisms (core to rim and along the prism length; Fig. 2C) and the different compositions of rosette-like CaREE-fluorcarbonates, may be due to either disequilibrium between the crystal and the liquid during grain growth (as commonly observed for plagioclase, for instance), or mutable liquid composition during crystallization, or leaching/deposition by a late metasomatic fluid. The zoning observed in synchysite-(Ce) prisms is inconsistent with a late metasomatic fluid, which would have affected homogeneously from the exterior to the interior the crystals along their length. Instead, the observed pattern is consistent with a fluid that changed composition during grain growth (Jessell, 2004), as well as with the relative higher facility to crystallize LREE CaREE-fluorcarbonates respect to their HREE-counterpart (Rodriguez-Blanco et al., 2014; Szucs et al., 2020), which therefore arises as the cause of disequilibrium. Indeed, Ce, La and Nd enter the crystal structure earlier than Y, which notably behaves as a HREE.

Synchysite-(Ce), both in rosettes or prisms, as well as the other fluorcarbonates, are often found included in the rims of euhedral quartz and feldspar or on them and on chamosite. Synchysite-(Ce) was also found included in fluorite. This means that all CaREE-fluorcarbonates morphologies and compositions crystallized in the latest stage of feldspar, quartz and chamosite crystallization or shortly after.

The pink colour of feldspar is commonly attributed to the presence of microscopic hematite inclusions deposited by post-magmatic hydrothermal fluids, which may also cause albitization of K-feldspar (Kaur et al., 2012). A Na-replacement in K-feldspar was actually observed towards the rim of the crystals (Fig. S3), and hematite is abundant within CaREE-fluorcarbonates. Therefore, even if we did not focus our TEM investigation on K-feldspar, we can reasonably assume that the vivid reddish colour of K-feldspar is due to metasomatism.

Albitization of feldspar and hydrothermal crystallization of quartz and chamosite may occur over a broad temperature range: albitization of feldspar between 350 and 450 °C (Kaur et al., 2012 and references therein); quartz crystallization between 100 and 700 °C (Rusk et al., 2008) and chamosite crystallization between 80 and 600 °C (Bourdelle, 2021; Fulignati, 2020). Thus, we can reasonably hypothesize an upper temperature limit of approximately 350–450 °C as the initiation of crystallization of CaREE-fluorcarbonates, with the different compositions and morphologies attributed to fluid fractionation under decreasing temperature.

Vallina et al. (2014), studying the hydrothermal crystallization of hydroxylbastnäsite-(Nd) ($NdCO_3OH$) at variable temperatures (165–220 °C), found that different shapes and crystal sizes can be obtained as function of temperature and heating rate. The more regular and idiomorphic morphologies (triangular pyramids and spine-shaped aggregates) were obtained when the supersaturation conditions were reached more slowly (at low temperature and slow heating rate), whereas more irregular cauliflower-like and fishbone (dendritic) morphologies were obtained when the supersaturation conditions were reached quickly. Analogous observations were made by Gai et al. (2014).

On the other hand, there is a relatively large body of evidence from hydrothermal syntheses of REE-carbonates indicating that the REEs composition influences the resulting crystal morphology. For instance, Rodriguez-Blanco et al. (2014) synthesizing REE-lanthanites ($REE_2(CO_3)_3{\cdot}8H_2O$) from aqueous solutions at ambient temperature, found that in all experiments lanthanites formed from a poorly ordered nanoparticulate precursor and that the differences in ion size and ionic potential as well as differences in dehydration energy of the REE^{3+} ions control the crystallization kinetics, unit-cell dimensions and morphology of the final crystalline lanthanites. In particular, lanthanites containing heavier REE^{3+} ions (Nd^{3+} or Pr^{3+}) developed smaller crystallites compared to their lighter La^{3+}- or Ce^{3+}-bearing counterparts. Moreover, while lanthanite-(La) developed well-formed and euhedral shapes, heavier REE^{3+}-bearing lanthanites (Ce, Pr and Nd) progressively developed more subhedral shapes with crystal imperfections (twinning).

Price et al. (2023) synthesizing La-Nd carbonates from aqueous solutions at 30 °C, found that the final (stable) pure La-, pure-Nd- and mixed La-Nd carbonates (in all cases lanthanite) had different morphologies and crystal sizes. As for Rodriguez-Blanco et al. (2014), they found that the precursor of lanthanite was an amorphous REE nanoparticle aggregate. Szucs et al. (2023) studying the crystallization of REEs carbonates at hydrothermal conditions (21–220 °C) through mineral replacement reactions, starting with dolomite and aragonite seeds, found that maintaining constant the parameters during the synthesis, notably the reaction temperature, duration and the nature of the seeds, the final morphology was different for different targeted REEs. At the highest investigated temperature range (165–220 °C), hydroxylbastnäsite ($REECO_3OH$) was the stable phase, while lanthanite was favored at lower temperatures (21–80 °C). Although all the above examples deal with simplified systems, lacking fluorine as component and employing only few REEs, it is reasonable to assume that in the more complex REEs-Ca-CO_3-F system, the composition of the fluid could, at least in part, control the morphology of the crystallizing REE carbonate.

In this work, synchysite-(Ce), other than included in quartz and feldspar, was also found included in fluorite. This may suggest that the fluid, initially high in Ca and F, reached the conditions for the crystallization of fluorite and synchysite-(Ce), subtracting Ca and entering into the conditions to crystallize bastnäsite-(Ce). The proposed sequence aligns with the Schreinemakers' analysis conducted by Williams-Jones and Wood (1992). They investigated the system $REE(CO_3)F$-$CaCO_3$-$F_2(CO_3)_{-1}$ to design a preliminary petrogenetic grid for CaREE-fluorcarbonates such as bastnäsite, synchysite, and parisite. This approach, based on chemographic analysis, is essential, as thermodynamic data are not yet available for all the phases involved. Among thirty-two different topological nets, Williams-Jones and Wood (1992) identified the one that best explained natural occurrences. The phase relations around the [cc] bundle, relevant to our discussion, are reproduced in Fig. 10. Our findings are consistent with the divariant field at low-*T* and low-*P* highlighted by the grey shadow. In this region, the phase diagram ($\log a Ca^{2+} \cdot a^2F^- $ vs. $\log a^2F^-/aCO_3^{2-}$) suggests that variations in the activities of Ca, CO_3, and F control phase relations, leading to the possible interconversion of one fluorcarbonate to another. This supports the stabilization of synchysite and then bastnäsite within similar *PT* conditions upon changing the activities of Ca, CO_3, or both.

In this scenario, bastnäsite-(Nd) is the last fluorcarbonate to crystallize, in agreement with thermodynamic studies (Gysi and Williams-Jones, 2015). Its "desert-rose" microstructure is consistent with a low temperature phase – desert rose is supposed to form in evaporitic environment at ambient conditions – and the nanoparticle structure may represent the nanoparticle precursors described in the experiments (Price et al., 2023; Rodriguez-Blanco et al., 2014; Vallina et al., 2014) that never matured into larger and regular crystals due to the low temperature, which hindered elemental diffusion and aggregation.

In summary, this scenario suggests: (i) synchysite-(Ce) prisms formed early in the crystallization sequence from a Ca- and F-rich fluid, at relatively low cooling rate; (ii) the Ca-depleted fluid then reached the condition to form blocky bastnäsite-(Ce), still at relatively low cooling rates; (iii) the fluid reached again, at slightly lower temperatures, supersaturation conditions for Ca and Ce, crystallizing rosette-like synchysite-(Ce). Indeed, so many "petals" of synchysite-(Ce) may represent fast nucleation events under a relatively high cooling rate that resulted

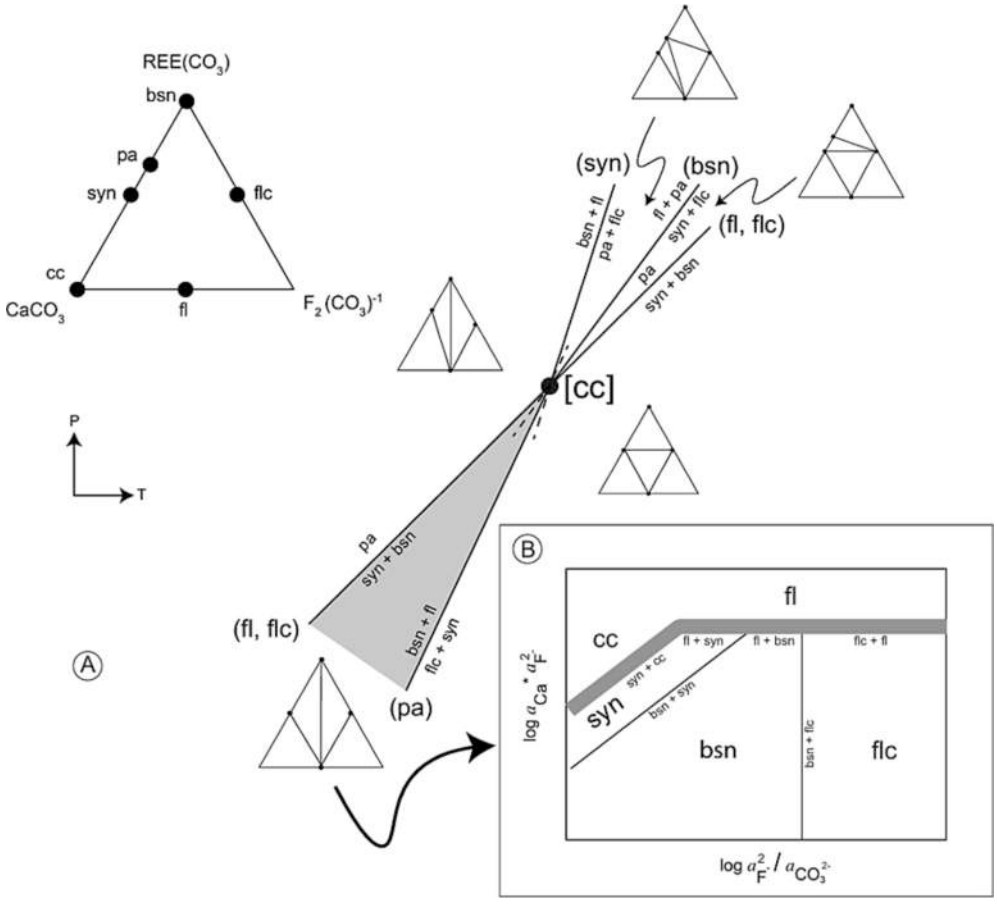

Fig. 10. (A) *P-T* net around the bundle [cc] showing phase relations at low-*T* and low-*P* in the $REE(CO_3)F$-$CaCO_3$-$F_2(CO_3)_{-1}$ system (bsn = bastnäsite, syn = synchysite, fl = fluorite, flc = fluocerite, cc = calcite, pa = parisite). (B) Schematic isobaric-isothermal $\log(aCa^{2+} \cdot a^2F^-)$ vs. $\log(a^2F^-/aCO_3^{2-})$ diagram corresponding to the shaded divariant phase field in (A). It can be seen that crystallization may switch from synchysite to bastnäsite by decreasing the activity of Ca^{2+} and F^- while keeping constant the a^2F^-/aCO_3^{2-} ratio, and vice versa (from Williams-Jones and Wood, 1992, modified).

into undeveloped prisms; (iv) the remaining fluid, at that point depleted in Ca and Ce and at low temperature, crystallized rosette-like bastnäsite-(Nd). The scaffold nanostructure made of bastnäsite-(Nd) nanocrystals walled by solid synchysite-(Ce) may suggests that the hydrothermal fluid supersaturation conditions oscillated slightly between those suitable for the crystallization of bastnäsite-(Nd) and those suitable for synchysite-(Ce).

Kaolinite, notably a low temperature phase (Erkoyun and Kadir, 2011; Marumo, 1989; Yuan et al., 2014), intergrown with CaREE-fluorcarbonates, may represent the residue of the silicate fluid deriving from the leaching of primary feldspars and iron-rich phases of the granophyre and associated volcanic rocks. The presence of these phyllosilicates, and hematite, may have hampered (physically) the development of larger single crystals of bastnäsite-(Nd). The bastnäsite nanostructure is also consistent with the fact that Nd-carbonate is more difficult to crystallize than LREE-carbonates, and usually leads to smaller crystals (Rodriguez-Blanco et al., 2014; Szucs et al., 2020). Moreover, the bastnäsite-(Nd) nanoparticles closely resemble the REE-nanoparticle aggregate precursors often observed experimentally (e.g. Price et al., 2023; Rodriguez-Blanco et al., 2014; Vallina et al., 2014) and may represent the final morphology assumed at the end of crystallization under low temperature, high cooling rate and fast nucleation process from a supersaturated solution. Finally, Th sometimes observed in the rim of the CaREE-fluorcarbonate crystals, may derive from hydrothermal alteration of zircon and other accessory phases in the granophyre (e.g. thorite and monazite). It has been observed that Th is associated with Y (i.e. Y-Th zoning in hexagonal prism synchysite-(Ce)) and enters the crystal structure of CaREE-fluorcarbonates at the latest stage of crystallization.

CRediT authorship contribution statement

Roberto Conconi: Writing – original draft, Visualization, Investigation, Conceptualization. **Paolo Gentile:** Resources, Investigation. **Patrizia Fumagalli:** Writing – review & editing, Resources. **Fernando Nieto:** Writing – review & editing, Supervision, Resources. **Giancarlo Capitani:** Writing – original draft, Validation, Supervision, Resources, Conceptualization.

Declaration of competing interest

The authors declare that they have no known competing financial interests or personal relationships that could have appeared to influence the work reported in this paper.

Acknowledgments

This study was supported by FAQC (University Competitive Funds) 2022 “Carbon REE-Cycle” and by the Italian Ministry of University and Research (MIUR) through the “Dipartimenti di Eccellenza–2019” grants.

Maria del Mar Abad Ortega and Cecilia de la Prada Sanchez are greatly acknowledged for their help during TEM analysis at the Centro de Instrumentacion Cientifica of the University of Granada and Melissa Saibene for the help during sample cutting with the ultramicrotome at the PMiB. Caterina Capitani provided the graphical abstract. Constructive comments by Bernard Grobéty and two anonymous reviewers improved the manuscript.

Appendix A. Supplementary data

Supplementary data to this article can be found online at https://doi.org/10.1016/j.lithos.2025.108033.

References

Bakos, F., Del Moro, A., Visona, D., 1990. The Hercynian volcano-phitonic association of Ganna (Lake Lugano, Central Southern Alps, Italy). Eur. J. Mineral. 2, 373–384. https://doi.org/10.1127/ejm/2/3/0373.

Balaram, V., 2019. Rare earth elements: a review of applications, occurrence, exploration, analysis, recycling, and environmental impact. Geosci. Front. 10, 1285–1303. https://doi.org/10.1016/j.gsf.2018.12.005.

Boriani, A., Burlini, L., Caironi, V., Giobbi Origoni, E., Sassi, A., Sesana, E., 1988. Geological and petrological studies on the Hercynian plutonism of Serie Dei Laghi - Geologic map of its occurrence between Valsesia and Lago Maggiore (N-Italy). Rendiconti Società Italiana Mineralogia Petrologia 43, 367–384.

Bourdelle, F., 2021. Low-Temperature Chlorite Geothermometry and Related recent Analytical advances: a Review. Minerals 11, 130. https://doi.org/10.3390/min11020130.

Capitani, G., 2019. HRTEM investigation of bastnäsite–parisite intergrowths from Mount Malosa (Malawi): ordered sequences, polysomatic faults, polytypic disorder, and a new parisite-(Ce) polymorph. Eur. J. Mineral. 31, 429–442. https://doi.org/10.1127/ejm/2019/0031-2824.

Capitani, G., 2020. Synchysite-(Ce) from Cinquevalli (Trento, Italy): Stacking Disorder and the Polytypism of (Ca,REE)-Fluorcarbonates. Minerals 10, 77. doi: https://doi.org/10.3390/min10010077.

Capitani, G., Mugnaioli, E., Gentile, P., 2018. Submicrometer yttrian zircon coating and arborescent aeschynite microcrystals on truncated bipyramidal anatase: an electron microscopy study of miarolitic cavities in the Cuasso al Monte granophyre (Varese, Italy). Am. Mineral. 103, 480–488. https://doi.org/10.2138/am-2018-6242.

Ciobanu, C., Kontonikas-Charos, A., Slattery, A., Cook, N., Wade, B., Ehrig, K., 2017. Short-Range Stacking Disorder in Mixed-Layer Compounds: a HAADF STEM Study of Bastnäsite-Parisite Intergrowths. Minerals 7, 227. https://doi.org/10.3390/min7110227.

Conconi, R., Fumagalli, P., Capitani, G., 2023a. A multi-methodological study of the bastnäsite-synchysite polysomatic series: Tips and tricks of polysome identification and the origin of syntactic intergrowths. Am. Mineral. 108, 1658–1668. https://doi.org/10.2138/am-2022-8678.

Conconi, R., Ventruti, G., Nieto, F., Capitani, G., 2023b. TEM-EDS microanalysis: Comparison among the standardless, Cliff & Lorimer and absorption correction quantification methods. Ultramicroscopy 254, 113845. Doi: https://doi.org/10.1016/j.ultramic.2023.113845.

Demartin, F., Minaglia, A., Gramaccioli, C.M., 2001. Characterization of gadolinite-group minerals using crystallographic data only: the case of hingganite-(y) from Cuasso al Monte, Italy. The Canadian Mineralogist 39, 1105–1114. https://doi.org/10.2113/gscanmin.39.4.1105.

Erkoyun, H., Kadır, S., 2011. Mineralogy, micromorphology, geochemistry and genesis of a hydrothermal kaolinite deposit and altered Miocene host volcanites in the Hallaçlar area, Uşak, western Turkey. Clay Miner. 46, 421–448. https://doi.org/10.1180/claymin.2011.046.3.421.

Fagnani, G., 1946. Il porfido quarzifero di Cavagnano (Porto Ceresio). Atti della Società Italiana di Scienze Naturali 85, 85–96.

Förster, H.-J., 2001. Synchysite-(Y)-synchysite-(Ce) solid solutions from Markersbach, Erzgebirge, Germany: REE and Th mobility during high-T alteration of highly fractionated aluminous A-type granites. Mineralgy and Petrology 72, 259–280. https://doi.org/10.1007/s007100170019.

Fulignati, P., 2020. Clay minerals in hydrothermal systems. Minerals 10, 919. https://doi.org/10.3390/min10100919.

Gai, S., Li, C., Yang, P., Lin, J., 2014. Recent progress in rare earth micro/nanocrystals: soft chemical synthesis, luminescent properties, and biomedical applications. Chem. Rev. 114, 2343–2389. https://doi.org/10.1021/cr4001594.

Gysi, A.P., Williams-Jones, A.E., 2015. The thermodynamic properties of bastnäsite-(Ce) and parisite-(Ce). Chem. Geol. 392, 87–101. https://doi.org/10.1016/j.chemgeo.2014.11.001.

Jessell, M., 2004. Geometries of mineral zonation, the characteristic geometries of mineral zonation. In: Köhn, D., Malthe-Sørenssen, A. (Eds.), Numerical Modeling of Microstructures. Journal of the Virtual Explorer. Electronic Edition, ISSN 1441–8142, Volume 15, Paper 3.

Kaur, P., Chaudhri, N., Hofmann, A.W., Raczek, I., Okrusch, M., Skora, S., Baumgartner, L.P., 2012. Two-Stage, Extreme Albitization of A-type Granites from Rajasthan, NW India. J. Petrol. 53, 919–948. https://doi.org/10.1093/petrology/egs003.

Kuebler, K., Wang, A., Freeman, J.J., Jolliff, B.L., 2006. Database of Raman mineral spectra for planetary surface exploration. In: 37th Annual Lunar and Planetary Science Conference, 1907.

Liendo, F., Arduino, M., Deorsola, F.A., Bensaid, S., 2022. Factors controlling and influencing polymorphism, morphology and size of calcium carbonate synthesized through the carbonation route: a review. Powder Technol. 398, 117050. https://doi.org/10.1016/j.powtec.2021.117050.

Marumo, K., 1989. Genesis of kaolin minerals and pyrophyllite in Kuroko deposits of Japan: Implications for the origins of the hydrothermal fluids from mineralogical and stable isotope data. Geochim. Cosmochim. Acta 53, 2915–2924. https://doi.org/10.1016/0016-7037(89)90168-3.

Meng, D., Wu, X., Mou, T., Li, D., 2001a. Determination of six new polytypes in parisite-(Ce) by means of high-resolution electron microscopy. Mineralogical Magazine 65, 797–806. https://doi.org/10.1180/0026461016560010.

Meng, D., Wu, X., Mou, T., Li, D., 2001b. Microstructural investigation of new polytypes of parisite-(Ce) by high-resolution transmission electron microscopy. Can. Mineral. 39, 1713–1724. https://doi.org/10.2113/gscanmin.39.6.1713.

Meng, D., Wu, X., Han, Y., Meng, X., 2002. Polytypism and microstructures of the mixed-layer member B2S, CaCe3(CO3)4F3 in the bastnaesite-(Ce)–synchysite-(Ce) series. Earth Planet. Sci. Lett. 203, 817–828. https://doi.org/10.1016/S0012-821X(02)00947-0.

Migdisov, A.A., Williams-Jones, A.E., 2014. Hydrothermal transport and deposition of the rare earth elements by fluorine-bearing aqueous liquids. Miner. Deposita 49, 987–997. https://doi.org/10.1007/s00126-014-0554-z.

Migdisov, A., Williams-Jones, A.E., Brugger, J., Caporuscio, F.A., 2016. Hydrothermal transport, deposition, and fractionation of the REE: Experimental data and thermodynamic calculations. Chem. Geol. 439, 13–42. https://doi.org/10.1016/j.chemgeo.2016.06.005.

Newbury, D.E., Ritchie, N.W.M., 2015. Performing elemental microanalysis with high accuracy and high precision by scanning electron microscopy/silicon drift detector energy-dispersive X-ray spectrometry (SEM/SDD-EDS). J. Mater. Sci. 50, 493–518. https://doi.org/10.1007/s10853-014-8685-2.

Newbury, D.E., Ritchie, N.W.M., 2019. Electron-Excited X-ray Microanalysis by Energy Dispersive Spectrometry at 50: Analytical Accuracy, Precision, Trace Sensitivity, and Quantitative Compositional Mapping. Microsc. Microanal. 25, 1075–1105. https://doi.org/10.1017/S143192761901482X.

Ngwenya, B.T., 1994. Hydrothermal rare earth mineralisation in carbonatites of the Tundulu complex, Malawi: Processes at the fluid/rock interface. Geochim. Cosmochim. Acta 58, 2061–2072. https://doi.org/10.1016/0016-7037(94)90285-2.

Peiravi, M., Dehghani, F., Ackah, L., Baharlouei, A., Godbold, J., Liu, J., Mohanty, M., Ghosh, T., 2021. A Review of Rare-Earth elements Extraction with Emphasis on Non-conventional sources: coal and Coal Byproducts, Iron Ore Tailings, Apatite, and Phosphate Byproducts. Mining Metallurgy & Exploration 38, 1–26. https://doi.org/10.1007/s42461-020-00307-5.

Pezzotta, F., 2005. Scandium silicates from the Baveno and Cuasso al Monte NYF-granites, Southern Alps (Italy): Mineralogy and genetic inferences. Am. Mineral. 90, 1442–1452. https://doi.org/10.2138/am.2005.1478.

Pezzotta, F., Diella, V., Guastoni, A., 1999. Chemical and paragenetic data on gadolinite-group minerals from Baveno and Cuasso al Monte, southern Alps, Italy. Am. Mineral. 84, 782–789. https://doi.org/10.2138/am-1999-5-612.

Pinarelli, L., Boriani, A., Del Moro, A., 1993. The Pb isotopic systematics during crustal contamination of subcrustal magmas: the Hercynian magmatism in the Serie Dei Laghi (Southern Alps, Italy). Lithos 31, 51–61. https://doi.org/10.1016/0024-4937(93)90032-8.

Pinarelli, L., Moro, A.D., Boriani, A., Caironi, V., 2002. Sr,Nd isotope evidence for an enriched mantle component in the origins of the Hercynian gabbro-granite series of the "'Serie dei Laghi'" (Southern Alps, NW Italy). Eur. J. Mineral. 14, 403–415. https://doi.org/10.1127/0935-1221/2002/0014-0403.

Pouchou, J.L., Pichoir, F., 1991. Quantitative Analysis of Homogeneous or Stratified Microvolumes applying the Model "PAP". In: Heinrich, K.F.J., Newbury, D.E. (Eds.), Electron Probe Quantitation. Springer, Boston, MA. https://doi.org/10.1007/978-1-4899-2617-3_4.

Price, D.L., Butler, I.B., Ngwenya, B.T., Kirstein, L.A., McDermott, F., O'Neill, T., 2023. Crystallisation pathways of a mixed La Nd carbonate – Ambient temperature synthesis of the mineral lanthanite. Chem. Geol. 617, 121265. https://doi.org/10.1016/j.chemgeo.2022.121265.

Rodriguez-Blanco, J.D., Vallina, B., Blanco, J.A., Benning, L.G., 2014. The role of REE $^{3+}$ in the crystallization of lanthanites. Mineral. Mag. 78, 1373–1380. https://doi.org/10.1180/minmag.2014.078.6.03.

Rusk, B.G., Lowers, H.A., Reed, M.H., 2008. Trace elements in hydrothermal quartz: Relationships to cathodoluminescent textures and insights into vein formation. Geology 36, 547. https://doi.org/10.1130/G24580A.1.

Sovacool, B.K., Ali, S.H., Bazilian, M., Radley, B., Nemery, B., Okatz, J., Mulvaney, D., 2020. Sustainable minerals and metals for a low-carbon future. Science 367, 30–33. https://doi.org/10.1126/science.aaz6003.

Szucs, A.M., Stavropoulou, A., O'Donnell, C., Davis, S., Rodriguez-Blanco, J.D., 2020. Reaction Pathways toward the Formation of Bastnäsite: Replacement of Calcite by rare Earth Carbonates. Cryst. Growth Des. 21, 512–527. https://doi.org/10.1021/acs.cgd.0c01313.

Szucs, A.M., Maddin, M., Brien, D., Guyett, P.C., Rodriguez-Blanco, J.D., 2023. Targeted Crystallization of rare Earth Carbonate Polymorphs at Hydrothermal Conditions via Mineral Replacement Reactions. Global Chall. 7, 2200085. https://doi.org/10.1002/gch2.202200085.

Tazaki, K., 2005. Microbial Formation of a Halloysite-like Mineral. Clay Clay Miner. 53, 224–233. https://doi.org/10.1346/CCMN.2005.0530303.

Vallina, B., Rodriguez-Blanco, J.D., Blanco, J.A., Benning, L.G., 2014. The effect of heating on the morphology of crystalline neodymium hydroxycarbonate, NdCO $_3$ OH. Mineralogical Magazine 78, 1391–1397. https://doi.org/10.1180/minmag.2014.078.6.05.

Van Landuyt, J., Amelinckx, S., 1975. Multiple beam direct lattice imaging of new mixed-layer compounds of the bastnäsite-synchysite series. Am. Mineral. 60, 351–358.

Vidal, O., Goffé, B., Arndt, N., 2013. Metals for a low-carbon society. Nat. Geosci. 6, 894–896. https://doi.org/10.1038/ngeo1993.

Vignola, P., Hatert, F.D.R., Bersani, D., Diella, V., Gentile, P., Risplendente, A., 2012. Chukhrovite-(Ca), $Ca_{4.5}Al_2(SO_4)F_{13}{\cdot}12H_2O$, a new mineral species from the Val Cavallizza Pb–Zn–(Ag) mine, Cuasso al Monte, Varese province, Italy. European Journal of Mineralogy 24, 1069–1076. https://doi.org/10.1127/0935-1221/2012/0024-2247.

Wang, Z.-Y., Fan, H.-R., Zhou, L., Yang, K.-F., She, H.-D., 2020. Carbonatite-related REE deposits: an overview. Minerals 10, 965. https://doi.org/10.3390/min10110965.

Williams-Jones, A.E., Wood, S.A., 1992. A preliminary petrogenetic grid for REE fluorocarbonates and associated minerals. Geochim. Cosmochim. Acta 56, 725–738. https://doi.org/10.1016/0016-7037(92)90093-X.

Williams-Jones, A.E., Migdisov, A.A., Samson, I.M., 2012. Hydrothermal Mobilisation of the Rare Earth Elements - a Tale of "Ceria" and "Yttria.". Elements 8, 355–360. https://doi.org/10.2113/gselements.8.5.355.

Wu, X., Meng, D., Pan, Z., Yang, G., 1998. Transmission electron microscope study of new, regular, mixed-layer structures in calcium-rare earth fluorcarbonate minerals. Mineralogical Magazine 62, 55–64. https://doi.org/10.1180/002646198547468.

Xing, Y., Etschmann, B., Liu, W., Mei, Y., Shvarov, Y., Testemale, D., Tomkins, A., Brugger, J., 2019. The role of fluorine in hydrothermal mobilization and transportation of Fe, U and REE and the formation of IOCG deposits. Chem. Geol. 504, 158–176. https://doi.org/10.1016/j.chemgeo.2018.11.008.

Yuan, Y., Shi, G., Yang, M., Wu, Y., Zhang, Z., Huang, A., Zhang, J., 2014. Formation of a hydrothermal kaolinite deposit from rhyolitic tuff in Jiangxi, China. J. Earth Sci. 25, 495–505. https://doi.org/10.1007/s12583-014-0439-1.